Chemistry – A European Journal

ChemEurJ Chemistry Europe European Chemical Societies Publishing

RESEARCH ARTICLE

pH-Switchable Excited-State Dynamics of Iridium(III) Photosensitizers Bearing an N-Heterocyclic Imine-Functionalized 2,2'-Bipyridine

Sven Lempereur[1,2] | Felix Glaser[1] | Jonas H. Franzen[2] | Leon Schöndorf[2] | Michael Siedl[2] | Ludovic Troian-Gautier[1,3] | Fabian Dielmann[2]

[1]Institut de la Matière Condensée et des Nanosciences (IMCN), Molecular Chemistry, Materials and Catalysis (MOST), Université catholique de Louvain (UCLouvain), Louvain-la-Neuve, Belgium | [2]Institute of General, Inorganic and Theoretical Chemistry, Universität Innsbruck, Innsbruck, Austria | [3]Wel Research Institute, Wavre, Belgium

Correspondence: Ludovic Troian-Gautier (Ludovic.Troian@uclouvain.be) | Fabian Dielmann (fabian.dielmann@uibk.ac.at)

Received: 14 October 2025 | **Revised:** 27 November 2025 | **Accepted:** 8 December 2025

Keywords: iridium photosensitizers | protonation | excited-state | halide binding | spectroscopy

ABSTRACT

We report the design, synthesis, and comprehensive photophysical characterization of a new class of heteroleptic Ir^{III} complexes featuring a strongly electron-donating 4,4′-bis(N-heterocyclic imine)-2,2′-bipyridine (bpy-NHI) ligand. The bpy-NHI ligand was synthesized on a multigram scale *via* a seven-step sequence and fully characterized. Reaction with the dimer $[Ir(ppy)_2Cl]_2$ afforded the target complex $[Ir(ppy)_2(bpy\text{-}NHI)]^+$, whose electronic structure was probed by (spectro)electrochemistry as well as by steady-state and time-resolved spectroscopy. Compared to the parent $[Ir(ppy)_2(bpy)]^+$ complex, the new complex exhibits a significantly altered redox profile, including a novel irreversible oxidation at 0.4 V *vs* Fc^+/Fc and the absence of the typical bpy-centered reduction, consistent with the strongly electron-donating nature of the NHI substituents. The high basicity of the NHI substituents enabled modulation of the excited-state properties via protonation, leading to unusual excited-state dynamics where the metal-to-ligand charge-transfer state switches between bpy- and ppy-based character. In the protonated form, the complex is able to bind chloride ions, which was qualitatively detected by changes in the ground-state absorption of the complex. These findings establish bpy-NHI as a powerful and sensitive electron-rich ligand platform for modulating the photophysical and electrochemical properties of Ir(III) complexes, opening new opportunities for the design of photosensitizers with tailored excited-state properties.

1 | Introduction

Iridium(III) polypyridyl complexes represent cornerstone photosensitizers in photoredox catalysis [1–4], sensing [5], and optoelectronic devices [6, 7], owing to their strong visible-light absorption, high photostability, and long-lived triplet excited states. Their versatility arises from the ability to finely tune their redox and photophysical properties through ligand design. In particular, the modularity of cyclometalated and diimine ligands offers a powerful platform to engineer frontier orbital energies, excited-state dynamics, and emission characteristics [8–10]. As new challenges in photocatalysis demand sensitizers with tailored reduction/oxidation potentials, absorption profiles, and excited-state lifetimes, the development of novel Ir(III) complexes with tunable properties remains a vibrant area of research [11–14].

Among the prototypical examples, tris(2-phenylpyridine) iridium(III), $[Ir(ppy)_3]$, features intense absorption in the visible region primarily arising from a singlet metal-to-ligand

charge transfer (^{1}MLCT) transition [15]. Strong spin–orbit coupling efficiently funnels the excitation into a long-lived ^{3}MLCT state with microsecond lifetime, making [Ir(ppy)$_3$] an excellent photosensitizer. However, its homoleptic architecture restricts modulation of the HOMO–LUMO gap, thereby limiting opportunities to diversify photophysical properties and excited-state reactivity. This limitation has driven the development of heteroleptic complexes, in which electronically distinct ligands afford more sophisticated excited-state manifolds [8, 16].

In archetypal heteroleptic complexes such as [Ir(ppy)$_2$(bpy)]$^+$, abbreviated as **Ir-bpy**, the HOMO resides primarily on the Ir-centered t_{2g} orbitals with contributions from the phenyl π-system, while the LUMO is mainly localized on the bipyridine π^* orbital [17]. This spatial separation of frontier orbitals introduces new charge-transfer pathways, including metal-ligand-to-ligand charge transfer (MLLCT) and enables independent tuning of HOMO and LUMO energies by modulation of the 2,2'-bipyridine and 2-phenylpyridine ligands [8–10, 18]. Rational modifications at the cyclometalated (C^N) ligands primarily shift the HOMO, whereas functionalization of the diimine (N^N) ligand controls the LUMO [19]. Next to the long excited-state lifetime and high triplet energies, this spatial control represents a key advantage in tailoring iridium complexes for applications requiring precise redox potentials or emission wavelengths.

While electron-withdrawing substituents on bipyridine ligands have been widely studied to lower LUMO levels and increase the oxidizing power of the corresponding complexes, electron-donating groups remain comparatively underexplored despite their potential to modulate excited-state reduction chemistry [20]. Common donors such as dialkylamino, methoxy, or *tert*-butyl groups provide modest effects, far weaker than the influence of strongly withdrawing substituents such as CF_3 or NO_2 (Figure 1). Inspired by recent work from the Teets group on heteroleptic complexes bearing β-diketiminate ligands [21–24], as well as others on electronic modifications of bipyridine ligands [25, 26], we set out to expand this underdeveloped design space.

In this work, we introduce the N-heterocyclic imine (NHI) motif as strongly electron-donating substituents on the bipyridine scaffold [27, 28]. NHIs have previously proven their utility as powerful π-donating entities for stabilizing main-group and transition-metal compounds [29], yet their potential in photosensitizer design remains unexplored. For our ligand design, we selected an NHI with exceptional strong π-donor properties and incorporated it at the 4,4'-positions of the 2,2'-bipyridine to ensure maximal conjugation while minimizing steric hindrance at the metal center. By the combination of different spectroscopic techniques, a modulation of the excited state by the addition of acid was found and a change of the nature of the lowest excited state was identified, potentially allowing to use protons as external stimuli to switch the properties of **Ir-NHI**. We demonstrate that this NHI functionalization represents a powerful strategy to modulate the electronic properties of Ir^{III} complexes, paving the way toward next-generation photosensitizers with finely tuned excited-state reduction potentials.

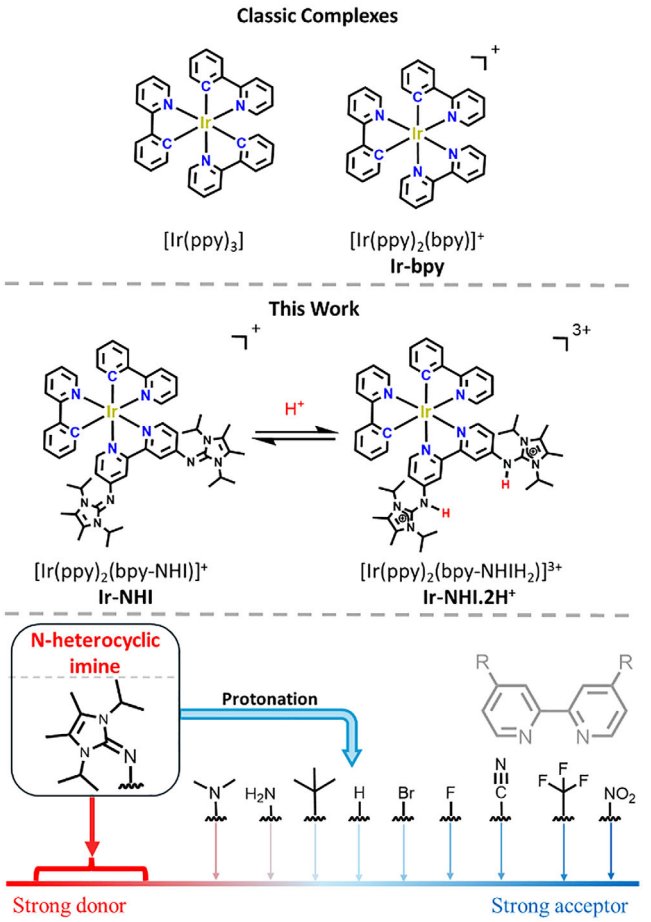

FIGURE 1 | Lewis structures of classical iridium(III) complexes (top) are shown alongside the new proton-responsive complex [Ir(ppy)$_2$(bpy-NHI)](PF$_6$) and its protonated derivative studied in this work (middle). At the bottom, a qualitative ranking of substituent effects on the donor properties of 2,2'-bipyridine ligands is shown.

2 | Results and Discussion

2.1 | Synthesis

The synthesis of the desired 4,4'-bis(NHI)-2,2'-bipyridine ligand (bpy-NHI) involves a seven-steps pathway starting from commercially available 2,2'-bipyridine (Figure 2a). The first step converted 2,2'-bipyridine into 2,2'-bipyridine-*N,N'*-dioxide using hydrogen peroxide in acetic acid [30, 31]. Subsequent nitration at the 4 and 4' position [30, 31], followed by phosphorus trichloride-mediated reduction [31], led to 4,4'-(NO$_2$)$_2$-2,2'-bipyridine. An *ipso*-substitution reaction with sodium azide produced 4,4'-(N$_3$)$_2$-2,2'-bipyridine,[32] which was then subjected to a modified Staudinger click-type reaction [32]. This step enabled the covalent attachment of a pre-synthetized carbene at the nitrogen atoms in both 4 and 4' positions, resulting in the targeted 4,4'-bis(NHI)-2,2'-bipyridine ligand. The synthesis was performed on a multigram scale, affording 8 g of the ligand, which was fully characterized using ^{1}H NMR, ^{13}C{^{1}H} NMR, 2D NMR spectroscopy (COSY, HSQC, HMBC), high resolution mass spectrometry (HRMS), and single crystal X-ray diffraction (SCXRD) analysis (see SI section 2 for details). The overall yield for the

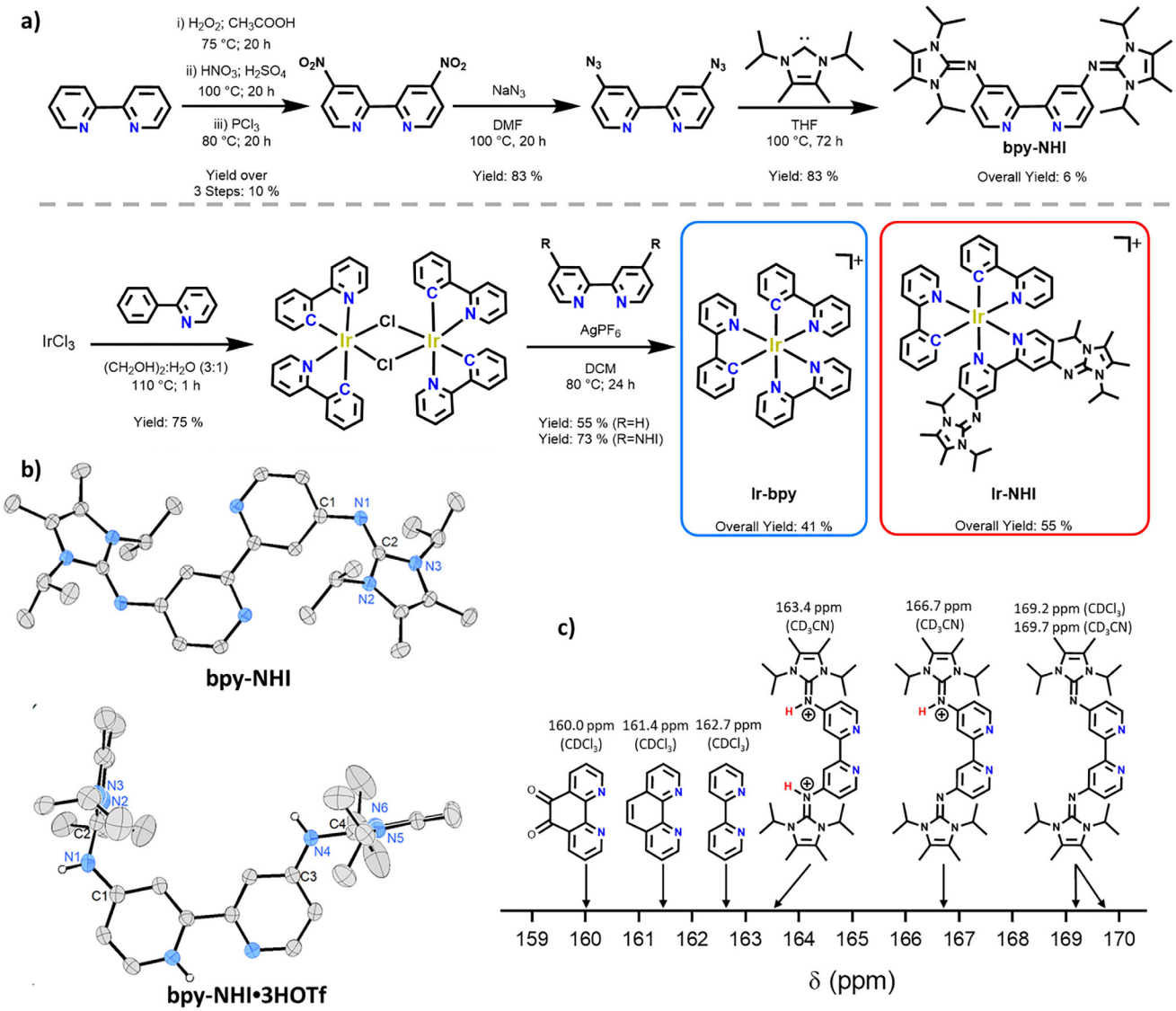

FIGURE 2 | (a) Top: Synthetic pathway starting from the commercial 2,2'-bipyridine, to the desired 4,4'-bis(NHI)-2,2'-bipyridine ligand. Bottom: two-steps synthetic pathway to obtain the desired heteroleptic iridium(III) complexes. Synthetic details are described in the supporting information in section 2. (b) Solid-state structure of bpy-NHI (top) and bpy-NHI•3HOTf (bottom) with hydrogen atoms (except the NH atoms) omitted for clarity; For bpy-NHI•3HOTf the triflate anions are also omitted for clarity. Selected bond lengths of bpy-NHI (Å): C1-N1 1.363(2), C3-N1 1.333(2), C3-N2 1.372(2), C3-N3 1.358(2). Selected bond lengths of bpy-NHI•3HOTf (Å): C1-N1 1.390(11), N1-C2 1.405(11), C2-N2 1.325(4), C2-N3 1.323(4),C3-N4 1.386(4), N4-C4 1.385(4), C4-N5 1.327(4), C4-N6 1.342(4). (c) Donor abilities of selected bidentate nitrogen ligands on the ^{13}C NMR spectroscopic scale (Huynh electronic parameter, HEP2, $CDCl_3$ at 77.7 ppm relative to TMS, CD_3CN at 118.3 and 1.3 ppm relative to TMS) [36]. Synthetic details and data are described in the supporting information in section 3.

synthesis of bpy-NHI was only 6% over the 7 steps, limited primarily by low yields in the 2,2'-bipyridine nitration and subsequent reduction steps in our laboratory. Notably, higher yields have been reported for those steps in the literature, which would raise the overall yield to ~27% over 7 steps (see SI section 2 for details).

The bpy-NHI ligand was then used to synthesize the target complex $[Ir(ppy)_2(bpy\text{-}NHI)](PF_6)$, abbreviated as **Ir-NHI** hereafter. In the first step, iridium(III) chloride hydrate ($IrCl_3 \cdot xH_2O$) underwent cyclometallation with 2-phenylpyridine at elevated temperatures, yielding the chloro-bridged dimer $[Ir(ppy)_2Cl]_2$ [33], which was engaged in the second step to coordinate the respective bipyridine ligand [20]. To facilitate chloride abstraction, the Ir(III) dimer was treated with $AgPF_6$. After workup, the desired complex **Ir-NHI** was isolated in 73% yield and was fully characterized by heteronuclear ^1H NMR, $^{13}C\{^1H\}$ NMR, ^{31}P NMR, ^{19}F NMR, 2D NMR spectroscopy (COSY, HSQC, HMBC), and HRMS (see SI section 2 for details).

Crystals of the free bpy-NHI ligand and of the protonated bpy-NHI•3HOTf ligand were subjected to SCXRD analyses (Figure 2b and SI section 5). Notably, the protonated ligand was obtained by treating bpy-NHI with 2,6-lutidinium triflate, highlighting the exceptional basicity of the bipyridine ligand, evidenced by its ability to accept three protons from 2,6-lutidine, an electron-rich

pyridine derivative itself. In the solid-state structure of bpy-NHI•3HOTf, both NHI substituents and one pyridine ring are protonated, with all three protons participating in hydrogen-bonding interactions with the triflate counteranions. The two pyridine rings adopt a chelating orientation toward the hydrogen atom, whereas in the case of the neutral bpy-NHI ligand an anti-parallel arrangement of the pyridine moieties is observed. The N—C bond lengths of the neutral bpy-NHI ligand (N1—C1: 1.363 Å. N1—C2: 1.333 Å, N2—C2: 1.372 Å, N3—C2: 1.358 Å) are comparable and fall between typical single (1.45 Å) and double (1.27 Å) bond distances [34, 35], consistent with the presence of a conjugated π-system. However, due to steric effects, the imidazoline ring and bipyridine units deviate significantly from planarity, with a dihedral angle of 53°, which reduces overall π-conjugation. In contrast, the tricationic bpy-NHI•3HOTf ligand exhibits significantly elongated exocyclic N—C bond lengths (1.385-1.405 Å) and shortened imidazoline N—C bonds (1.323-1.342 Å), consistent with the formation of cationic imidazolinium moieties. These imidazolinium groups are nearly orthogonal to the bipyridine unit, with dihedral angles of 85° and 89°. This structural arrangement further underscores the impact of protonation on the electronic and geometric properties of the ligand. Unfortunately, attempts to crystallize the final complex **Ir-NHI** were unsuccessful.

To assess the electronic properties of the bpy-NHI ligand, the ligand electronic parameter (HEP2) developed by the Huynh group was determined (Figure 2c) (see SI section 3 for details) [36, 37]. This parameter ranks the donor strength of bidentate ligands based on their influence on the ^{13}C chemical shift of the carbene carbon in a reporter complex of the type [PdBr(iPr_2-bimy)(XˆX)], where XˆX represents the bidentate ligand. The bpy-NHI ligand exhibits an HEP2 value of 169.2 ppm, indicating significantly stronger donor properties compared to the parent bipyridine (162.7 ppm). This result underscores the exceptional π-donor ability of the NHI groups, consistent with previous studies on *para*-NHI-substituted pyridines [27]. Upon protonation of the NHI groups, the donor strength of the ligand decreases progressively with each protonation step. The monocationic bpy-NHI•H^+ and dicationic bpy-NHI•$2H^+$ species exhibit HEP2 values of 166.7 ppm and 163.4 ppm in acetonitrile, respectively. These values reflect a stepwise reduction in donor strength, with the dicationic ligand displaying electronic properties comparable to those of the parent bipyridine. This trend highlights the sensitivity of the bpy-NHI ligand's electronic properties to protonation, as it directly affects the π-donor character of the NHI groups and thus enables remote tuning of the electronic nature of the bpy-NHI ligand through interaction with Lewis acids.

2.2 | Ground State Absorption Characterization and Stability Assessment

Ir-NHI was characterized by UV-visible absorption spectroscopy and electrochemistry. However, in initial photophysical measurements, data inconsistencies emerged, indicating a degree of chemical instability of the compound under ambient conditions. Therefore, the stability of **Ir-NHI** in solution was first studied in more detail under different conditions. A pivotal observation was the alteration of the UV–visible absorption spectra after exposing sealed vials of **Ir-NHI** in nondry acetonitrile to natural sunlight for several hours. In contrast, 72 hours under the same atmosphere and solvent but kept in the dark showed no change in the spectra and hence no sign of degradation (see SI section 6.1 Figure S41). To investigate the origin of this apparent instability or elevated reactivity, a series of spectroscopic studies were performed under controlled conditions. Three primary hypotheses were considered: i) degradation of the complex, ii) oxidation of the ligand due to the reaction with molecular oxygen dissolved in the solvent and iii) protonation of the ligand due to residual water present in the solvent.

A series of UV–visible absorption measurements were conducted using **Ir-NHI** in dry acetonitrile using different atmospheric conditions including argon, air, carbon dioxide, oxygen and nitrogen atmospheres, with continuous irradiation using a 447 nm continuous wave (cw) laser source at an intensity of 200 mW. Absorption spectra were recorded after different time intervals of irradiation to monitor changes induced by light exposure over time. A comparative analysis was carried out between **Ir-NHI** and the reference complex **Ir-bpy**. For **Ir-bpy**, no changes were detectable within these measurements (see SI section 6.1 Figure S40 and Table S3 for details) whereas significant changes were observed for **Ir-NHI** (Figure 3a and b). To quantify the modifications observed in the UV–visible absorption spectra, the half lifetime and the quantum yield of the reaction was calculated (Table S3) based on the assumption that a sole photoproduct is cleanly formed and that the same degradation pathway occurs under all investigated conditions. Under an oxygen atmosphere or air, a significant change within the first 60 seconds of irradiation was observed, indicating a significant photo-instability under these conditions. Calculation of the quantum yield for this process indicated values around 1.8% and 3.4% under air and oxygen atmosphere, respectively (see SI section 6.7). In addition, analogous experiments were performed in the presence of ~20 equivalents of triflic acid added prior to irradiation. Under these conditions a perfect stability of both complexes under irradiation was observed, with no change of the spectral features over the investigated irradiation time range. Usually iridium complexes are considered photostable, while in specific cases also others have observed instabilities with iridium photosensitizers [38, 39].

The results clearly demonstrate that both the simultaneous presence of oxygen and light are the main contributors to the degradation of **Ir-NHI**, as no decomposition occurred under Argon or carbon dioxide atmosphere or under air in the absence of irradiation. Consequently, all subsequent experiments were conducted under an inert atmosphere to prevent oxidative degradation. Additionally, as mentioned earlier, upon protonation of **Ir-NHI** to obtain the corresponding **Ir-NHI.2H$^+$**, the stability of the complex under combined light and oxygen exposure is restored (Table S3). This implies that the degradation most probably occurs on the imine fragment, which is protonated upon acid addition and consequently the degradation is not occurring anymore. This aspect will also be discussed below in more detail.

After identifying the key parameters influencing the stability of **Ir-NHI**, we then focused on the comprehensive characterization of the complexes. As discussed previously, a key advantage of the 4,4'-bis(NHI)-2,2'-bipyridine ligand is its ability to undergo protonation at the imine position, thereby allowing modulation

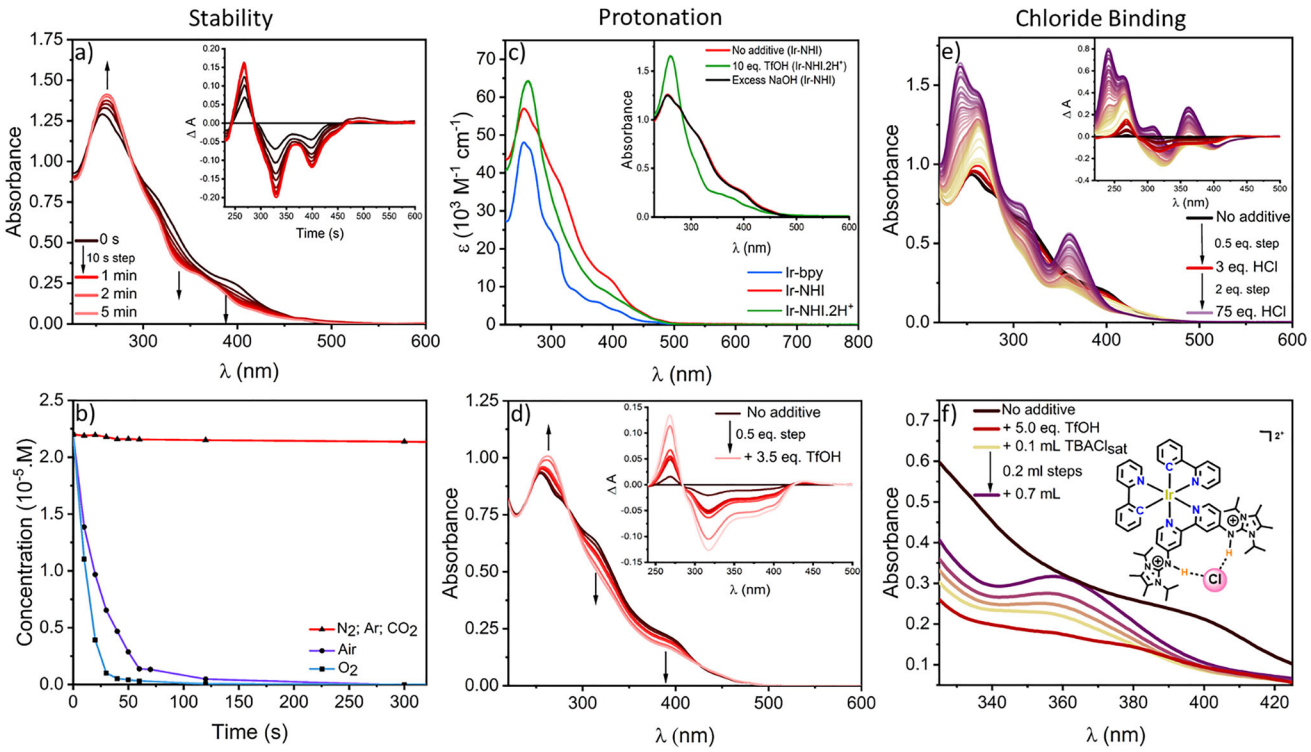

FIGURE 3 | UV–visible absorption spectra (a), difference absorption spectra (inset) under air and concentration changes over time under different conditions (b) of **Ir-NHI** (~30 μM) in acetonitrile recorded during continuous irradiation with a 447 nm cw laser with an intensity of 200 mW. For (b) the conditions are indicated. (c) UV-Visible absorption spectra of **Ir-bpy**, **Ir-NHI** and **Ir-NHI.2H**$^+$ recorded in acetonitrile. The inset represents the reversibility test upon protonation with triflic acid (TfOH) and subsequent deprotonation with excess of base. (d) Stepwise protonation of **Ir-NHI** by the stepwise addition of TfOH. (e) UV-visible absorption spectra upon titration of HCl to solutions of **Ir-NHI** (~20 μM) in acetonitrile, where protonation effects are highlighted in red. (f) Stepwise titration using separate additions of TfOH (proton source) and TBACl (chloride source), allowing individual assessment of H^+ and Cl^- effects, alongside a plausible molecular structure illustrating chloride binding.

of their electron-donating properties. However, this tunability also presents a challenge: the ligands are prone to spontaneous protonation or hydrogen bonding in the presence of traces of moisture. Even traces of water in nonanhydrous acetonitrile induced subtle shifts in the absorption spectra, indicating small amount of partial protonation. To address this issue, all spectroscopic and electrochemical measurements were conducted in rigorously anhydrous acetonitrile, using flame-dried glassware operating under an inert argon atmosphere. For experiments investigating the **Ir-NHI** complex in the nonprotonated form, 20 eq. of a aqueous solution of sodium hydroxide were added directly to the dry acetonitrile solutions and the solutions were filtrated. Upon treatment with hydroxide, slight spectral changes were observed by UV-visible absorption spectroscopy after the addition, likely due to residual protonation from traces of HCl in dichloromethane, i.e. the solvent used during the synthesis. Note that the use of alkaline water is only expected to lead to deprotonation, without introducing similar issues as those noted previously though the addition of water. The use of organic bases, such as amines, would have led to excited-state quenching that is not possible with sodium hydroxide using these type of photosensitizers.

Across the ultraviolet to visible spectrum of **Ir-bpy** (Figure 3c), several distinct absorption bands are observed with global or local maxima and shoulders centered around 250, 300, 400 nm [8]. **Ir-NHI** exhibited a similar absorption pattern, but the extended conjugation introduced by the NHI substituent reduced the energy gap for the ligand-centered π–π^* transition, increasing the proportion of $LC_{N^{\wedge}N}$ character relative to charge-transfer transitions and thereby enhancing the molar absorption coefficient (ε) around 380 nm. Interestingly, the molar absorption coefficient of the **Ir-NHI** complex is larger over the full spectral range in comparison to the reference compound **Ir-bpy**.

To further explore the influence of the imine protonation on the photophysical properties, titrations were conducted using various acids, i.e. aqueous hydrochloric acid (HCl), trifluoroacetic acid (TFA), triflic acid (TfOH) and ammonium hexafluorophosphate (NH_4PF_6). To confirm that the photophysical modifications were induced by the protonation on the NHI-substituent of the modified bipyridine, **Ir-bpy** was also analyzed under the same conditions. Indeed, for this reference complex no changes upon addition of acid were detectable (see SI section 6.2 Figure S42).

As illustrated in Figure 3d, the addition of triflic acid induced distinct changes in the absorption spectrum of **Ir-NHI**, more specifically a decrease in the intensity of the MLCT, LLCT, and ILCT absorption bands, alongside an increase in absorption in the π–π^* transition region. Stepwise titration of **Ir-NHI** with TfOH revealed the absence of spectral changes after the addition of 3.5 eq. of acid (see SI section 6.2 Figure S44), indicating full protonation at this point. It appears that protonation of the bridging nitrogen effectively decouples the π-system of the

NHI substituents from the bipyridine ligand and disrupts the previously discussed $LC_{N^{\wedge}N}$ contribution, leading to an absorption similar to the parent **Ir-bpy** complex, although with slightly larger molar absorption coefficients compared to the reference (Figure 3c). When aqueous HCl was used as a proton source, additional spectral changes were detectable in the absorption spectra as shown in Figure 3e (see SI section 6.2 Figure S45). Upon the addition of more than three equivalents, a new absorption band emerged around 360 nm, suggesting further structural or electronic changes after the initial protonation steps. A possible role of the water intrinsically present by the addition of this acid was excluded by reference measurements with addition of up to 100 equivalents of water without spectral changes (see SI section 6.2 Figure S43). We hypothesized that the chloride anion could play a role following protonation by comparison with similar systems reported by Meyer [40–44] and Beer [45–47], where chloride binding with transition metal complexes was investigated. To differentiate the effects of protons and chloride ions, stepwise titration experiments were carried out for **Ir-NHI** using triflic acid as a proton source and subsequent addition of tetra-*N*-butylammonium chloride (TBACl) as a chloride source (Figure 3f). Upon titration of chloride ions to a solution of **Ir-NHI** before the addition of the proton source, essentially no change was observed in the spectral region around 360 nm. However, upon titration of a saturated solution of TBACl to a complex already protonated by the presence of 5 equivalents of triflic acid, the characteristic absorption band centered around 360 nm appeared that was similar to the titration with aqueous HCl (Figure 3e). This stepwise formation of the chloride-specific complex confirms the cooperative effect between protonation and chloride in this complex. From the UV-visible **Ir-NHI** HCl titration, a chloride binding constant of 200 M^{-1} was extracted.

2.3 | Electrochemistry

Cyclic voltammetry (CV) was conducted on the free ligands as well as on the corresponding complexes and the results are summarized in Table 1. The measurements in acetonitrile revealed that the bpy-NHI ligand exhibited a more negative first reduction potential than the unsubstituted 2,2'-bipyridine. In addition, bpy-NHI exhibited an additional oxidation peak at 0.40 V vs Fc^+/Fc whereas no oxidation peak could be observed for the unsubstituted 2,2'-bipyridine ligand. The oxidation of the bpy-NHI ligand, which most likely occurs at the exocyclic nitrogen lone pair, was only partially reversible at high scan rates (>1 V/s) and was irreversible at slower scan rates (see SI section 6.4 Figure S48). This lone pair does not participate in the extended π-conjugation of the ligand. As a result, the corresponding radical cation lacks efficient charge delocalization, rendering the oxidized species thermodynamically less stable and more susceptible to irreversible degradation.

For the complexes, two clear general observations can be outlined when comparing **Ir-bpy** with **Ir-NHI**. First, the introduction of the bpy-NHI ligand leads to the appearance of a novel irreversible oxidation peak at 0.4 V *vs* Fc^+/Fc, as discussed earlier. The bpy-centered reduction at −1.8 V *vs* Fc^+/Fc for **Ir-bpy** completely disappeared for **Ir-NHI**, in line with the more electron-rich character of the bpy-NHI ligand. In addition, a slight anodic shift in the Ir(IV)/Ir(III) potential was observed (Figure 4), also

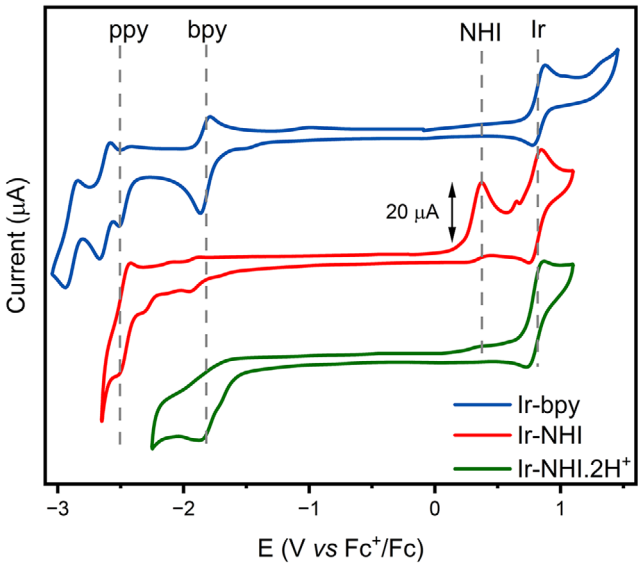

FIGURE 4 | Cyclic voltammograms of **Ir-bpy** (blue), **Ir-NHI** (red) and **Ir-NHI.2H$^+$** (green) recorded in acetonitrile in the presence of 100 mM of $TBAPF_6$ as electrolyte with a scan rate of 100 mVs^{-1}. **Ir-NHI.2H$^+$** (green line) was generated upon the addition of 3.0 equivalent of TfOH.

in line with the increased electron density at the metal center, rendering its oxidation more easily accessible. However, this shift is smaller than expected given the substantially greater donor strength of bpy-NHI ligand. We attribute the attenuated shift to the initial ligand-centered oxidation on the bpy-NHI scaffold, which diminishes its electron-donating ability prior to iridium oxidation, thereby masking the intrinsic impact of bpy-NHI on the Ir(IV)/Ir(III) potential.

To evaluate the effect of protonation, titrations with triflic acid were performed, ranging from 0.5 to 10 equivalents in acetonitrile and subsequently cyclic voltammograms were recorded (see SI section 6.3 Figure S46 and S47). A parallel experiment was conducted with the unsubstituted complex to confirm that the observed changes are specific to the modified ligands. Upon complete protonation, the first oxidation event associated with the NHI moiety entirely disappeared (Figure 4). This is in perfect agreement with the conclusion from absorption and NMR measurements (see SI section 4.1 Figure S33 and S34). suggesting a protonation of the NHI moiety, which then prevents the oxidation of the imine group. On the other hand, the reduction corresponding to the bipyridine shifts and is located in the protonated form at around ∼−1.8 V *vs* Fc^+/Fc, which is in fact the same as for the unsubstituted **Ir-bpy**, indicating that the protonation removes the effect of the attached NHI and decouples this structural moiety from the bpy.

2.4 | Excited-State Characterization

To comprehensively investigate the excited-state landscape of **Ir-NHI**, three complementary time-resolved spectroscopic techniques were used, namely time-correlated single photon counting (TCSPC), nanosecond transient-absorption spectroscopy (ns-TA spectroscopy), and femtosecond transient-absorption spec-

TABLE 1 | Ground- and Excited state Properties of **Ir-bpy**, **Ir-NHI** and **Ir-NHI.2H**$^+$.

Compound	E_{red} (V *vs* Fc^+/Fc)	E_{ox} (V *vs* Fc^+/Fc)	$\lambda_{max,\,abs}$ (nm); ε (10^3 M^{-1} cm^{-1})	$\lambda_{max,\,em}$, (nm)	$\lambda_{max,\,em,\,77K}$ (nm); E_{00} (eV)	ϕ[e]	τ (ns)[e]
bpy[a]	−2.67[b] [48]	2.45 (irr.)[d] [49]	282 (11) [50]	350 [50]	–	–	–
bpy-NHI[c]	< −2.85 (irr.)	0.40 *NHI* (irr.)	320 (37)	550	495 (2.50)	–	–
Ir-bpy[c]	−1.80 *bpy* (−2.46) (−2.63) (−2.89)	0.85 $Ir^{IV/III}$	255 (48) 300 (25) 380 (6)	595	505 (2.46)	0.035[51]	313
Ir-NHI[c]	−2.40 *ppy*	0.44 *NHI* (irr.) *(0.80 $Ir^{IV/III}$)*	256 (57) 308 (39) 385 (13)	540	479 (2.59)	0.002	0.3
Ir-NHI.2H$^+$[c]	∼−1.80 *bpy* (irr.)	0.85 $Ir^{IV/III}$	263 (66) 380 (10)	595	508 (2.44)	0.049	100

Electrochemically irreversible processes are denoted with (irr).

[a]Measurements performed in DMF containing 0.1 M $TBAPF_6$ at a scan rate of 500 mV s^{-1}.

[b]Measurements performed in THF containing 0.1 M $TBAPF_6$ at a scan rate of 100 mV s^{-1}.

[c]Measurements performed in acetonitrile containing 0.1 M $TBAPF_6$ at a scan rate of 100 mV s^{-1}.

[d]Measurements performed in acetonitrile containing 0.1 M Bu_4NClO_4 at a scan rate of 100 mV s^{-1}.

[e]Measurements performed in ACN and Argon atmosphere by relative actinometry using $[Ru(bpy)_3]^{2+}$ in ACN with a 0.095 (argon) and 0.018 (air) as a reference [52].

troscopy (fs-TA). The following measurements were performed under argon and in dry acetonitrile to prevent stability issues during the measurement, as discussed earlier.

The photophysical investigation of **Ir-bpy** has received significant attention over the past decade, as researchers aimed to resolve the distinct excitation and deactivation pathways involved in the decay of the excite state of heteroleptic iridium complexes [53, 54]. Based on the extensive literature, some assignments and rate constants were not investigated herein for **Ir-bpy** and solely assigned based on these prior reports. Upon excitation of **Ir-bpy** in deaerated acetonitrile at 270, 310, 400, or 450 nm, identical emission spectra were recorded at room temperature, only varying in their respective intensity due to the difference in absorbance at the excitation wavelength and all exhibiting a maximum emission wavelength at 595 nm as indicated by the dashed blue line in Figure 5a. This observation is consistent with the literature [8, 9, 55], as well as with Kasha's rule, resulting in a constant λ_{max} of emission regardless of the excitation energy. This photoluminescence decayed mono-exponentially with an excited-state lifetime of 63 ns under air and 313 ns under argon, also consistent with the literature [55]. Lastly, photoluminescence was recorded in a butyronitrile matrix at 77 K, leading to the triplet excited state energy of the investigated system with a corresponding value of 2.46 eV (Figure 5a).

Ir-bpy was also analyzed by femtosecond transient absorption spectroscopy with an excitation at 343 nm in anhydrous acetonitrile under argon. The results from a global fitting of the spectroscopic data with a sequential model utilizing one excited state and a corresponding hot state is represented in Figure 5d, where an excited-state absorption band with a global maximum around 500 nm and a broad side band above 650 nm are clearly detectable. The relative population from the global analysis is presented as inset. Chergui and co-workers previously used ultrafast transient absorption spectroscopy to disentangle the different short-lived nonemissive processes, corresponding to the formation of the $^3MLCT_{bpy}$ state from the $^3MLCT_{ppy}$, and our lifetime of 1 ps is in line with the reported lifetime of 1.5 ps [54]. Hence, it can be concluded that all processes populating the $^3MLCT_{bpy}$ state like the $^3MLCT_{ppy}$ are occurring within fs and early ps timescale and the $^3MLCT_{bpy}$ has a lifetime of several hundred nanoseconds under argon, as discussed below.

Nanosecond transient absorption spectroscopy of **Ir-bpy** in acetonitrile upon excitation at 420 nm revealed a positive excited-state absorption band around 380 nm together with a broad absorption with a maximum around 500 nm, indicative of absorption from the triplet excited state (Figure 5g). In line with other iridium complexes, a ground-state bleach is not visible due to the new excited-state absorption outcompeting this spectral feature, which should cause a negative signal in the differential absorbance spectrum [56, 57]. Spectroelectrochemical measurements were performed to attempt to model the transient absorption signature (see SI section 6.5 Figure S49). The electrochemical reduction of the bipyridine ligand, achieved by applying a potential of –1.6 V vs Fc^+/Fc, produced an absorption band centered around 380 nm as well as a gradually increasing absorption band with a local maximum around 530 nm, which is in good agreement with the transient absorption spectrum (Figure 5g). In contrast, the oxidation of the iridium center was not distinctly observed in the visible region, where signals are typically expected above 600 nm. These spectroelectrochemical observations support the assignment of the excited state as a $^3MLCT_{bpy}$ state, characterized by a reduced bipyridine moiety and an oxidized iridium center and the (small) differences are likely caused by more delocalized HOMO and LUMO in the excited state compared to the spectroelectrochemical measurements.

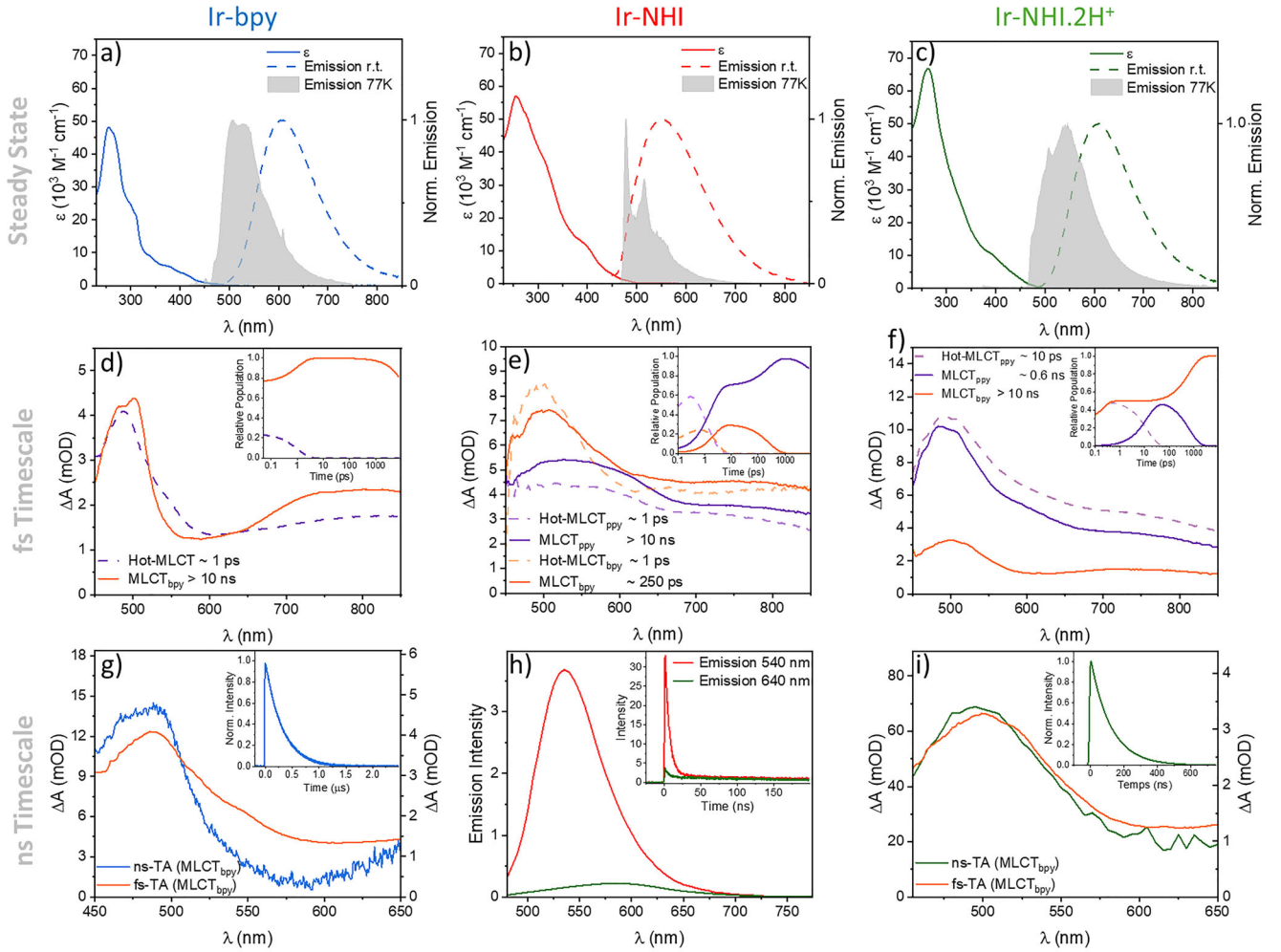

FIGURE 5 | UV-vis absorption (solid line) and emission (dashed line) in acetonitrile and frozen matrix (77 K) emission in butyronitrile (filled grey area) of **Ir-bpy** (a, blue), **Ir-NHI** (b, red) and **Ir-NHI.2H$^+$** (c, green). (d-f) Species-associated decay spectra and relative population (inset) for the evolution over time based on fitting by target analysis of the spectroscopic data obtained by femtosecond TA-spectroscopy of **Ir-bpy** (d), **Ir-NHI** (e) and **Ir-NHI.2H$^+$** (f) in acetonitrile excited at 343 nm (300 nJ). (g) Transient absorption (TA) spectrum of **Ir-bpy** (20 µM) detected 10 ns after the laser pulse at 420 nm, time-integrated over 200 ns. For comparison to the long-lived component from target analysis with fs-TAS is provided as a orange line and the kinetic trace on the µs timescale is shown as an inset. (h) Global analysis results of kinetic emission map for **Ir-NHI** recorded by time-resolved emission spectroscopy (TRES) with 5 nm steps between the kinetic traces analyzed with a parallel model. The traces at the emission maximum of the two components are shown as inset. (i) Global analysis result for the time-resolved kinetic absorption between 450 and 650 nm by ns-TAS with a monoexponential decay model for **Ir-NHI.2H$^+$** in ACN under air. For comparison to the long-lived component from target analysis with fs-TAS is provided as an orange line. Further details are discussed in the main text and further figures are presented in the SI section 6.6 and 6.8.

Ir-NHI was also photophysically characterized in dry acetonitrile, and the absorption and emission spectra are summarized in Figure 5b. Due to the efficient protonation (see Figure 3d) the samples were pretreated with base to ensure deprotonation. The limited photostability under air made some of the measurements challenging. The steady state emission clearly shows an emission with a maximum centered around 540 nm, which is weaker and significantly blue-shifted compared to the **Ir-bpy**. Emission kinetics at different detection wavelengths for a sample pretreated with NaOH were measured and highlighted a biexponential emission, with two components that have different contributions depending on the wavelength. Closer analysis of the wavelength-dependent emission kinetics under Argon by time-resolved spectroscopy revealed a short component (<~5 ns) centered around 540 nm together with a red-shifted emission centered around 580 nm with a lifetime of ~380 ns (Figure 5h) based on the global analysis with a parallel fitting model. Based on these spectral features, the short-lived emission is assigned to the **Ir-NHI**, while the long-lived component is tentatively assigned to traces of protonated **Ir-NHI.H$^+$** or **Ir-NHI.2H$^+$**. This protonated state is expected to have a minor contribution, which is in line with the fact that its contribution is hardly visible by steady-state emission spectroscopy (Figure 5b) and that the decay associated spectrum is significantly smaller than the short-lived component (Figure 5h), despite a significant drop in the general emission intensity of the signals, indicating much smaller emission quantum yield for the **Ir-NHI** compared to **Ir-bpy** or **Ir-NHI.2H$^+$**. An additional short-lived species cannot be reasonably well resolved by either the time-correlated single photon counting TCSPC technique under conditions for the TRES (Figure 5h) nor the nanosecond laser setup, where a kinetic map in the visible range was unsuccessful. Indeed, the short lifetime falls

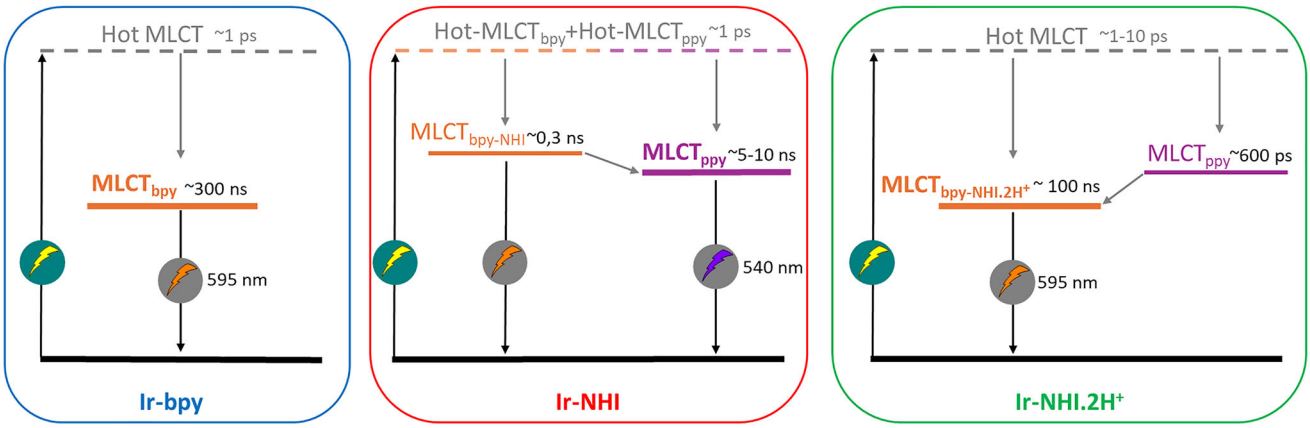

FIGURE 6 | Proposed photophysical scheme of **Ir-bpy** (left), **Ir-NHI** (middle) and **Ir-NHI.2H$^+$** (right) following visible light excitation.

within the instrument response function (IRF) of the nanosecond transient absorption setup and the combination of a very short and long lifetime under Argon prevents deconvolution on the TCSPC instrument on the two-microsecond-window. Under air, the lifetimes are shorter and when focusing on a 50 ns time window (see SI section 6.6 Figure S53) a short-lived component with a lifetime of 0.3 ns can be detected together with long-lived components of ~10 ns and ~80 ns, with the longest component being again assigned to traces of the protonated version, as discussed before. Due to the very mild conditions of the excitation light source, photoinstability is expected here to have a negligible role under these specific conditions. In fact, the early nanosecond emissive lifetimes are unusually short for an iridium-based complex, which typically exhibits microsecond-scale lifetimes due to the spin forbitten transition from the ^{3}MLCT to the ground state after efficient intersystem crossing facilitated by the heavy metal center. The relative amplitude (Figure 5h) of emission intensity in the parallel model used to fit the TRES dataset indicated a much larger relative intensity of the short-lived component despite the significantly shorter lifetime and about 25 times smaller emission quantum yield (0.002) compared to the emission of the protonated form (0.049), indicating a very minor amount of protonated complex, being in perfect agreement with the steady-state measurements (Figure 5b) that are dominated by the emission centered around 540 nm. No pretreatment of a solution of **Ir-NHI** in acetonitrile with NaOH resulted in a larger contribution of the red-shifted component in TCSPC measurements of the long-lived emissive excited state compared to the short-lived one. However, a complete shut-down of the red-shifted emission was not achieved even with the pretreatment with base. Spectral differentiation between the 0.3 ns and ~5-10 ns component was not successful by TCSPC techniques. Gratefully, ultrafast transient absorption measurements provided the resolution to successfully further disentangle the short-lived processes, although the stability of the sample under these conditions asks for an interpretation with some care. The best fit was obtained by target analysis with a branched deactivation pathway, resulting in one final longer-lived excited state (Figure 5e and Figure 6b). Both branches have a short-lived (~1 ps) hot state and the second branch [58], with an excited-state lifetime of ~250 ps, has a weak relative contribution of around 30% (orange color in Figure 5e). This lifetime is in reasonable agreement with the short-lived emission observed by TCSPC. In addition, the spectral feature, with a maximum centered around 500 nm and a broad tailing absorbance above ~600 nm, closely resembles the long-lived ^{3}MLCT from the **Ir-bpy** (as shown as blue trace in Figure 5g) and is thus reasonably assigned to an MLCT$_{bpy}$ state. This intermediate excited state populates the longer-lived (>10 ns) component, which is assigned to a MLCT$_{ppy}$-type excited state as the lowest emissive state [59]. This is in agreement with the first reduction in **Ir-NHI**, which is a ppy-centered reduction as the NHI moiety significantly influences the bpy reduction due to the strong electron donating character of the NHI moiety. Contributions from protonated complex were not identified within this analysis, highlighting again its very minor proportion. Focusing on ns-TAS, a weak, 20 ns long-lived signal is detectable (see SI section 6.6 Figure S52) which is in reasonable agreement with the fs-TA dataset, despite the fact that the nanosecond transient absorption spectrum tails less far into the red region (up to ~600 nm) compared to the long-lived species obtained by fs-TAS (up to ~650 nm). We assign this difference in the variation of concentration between the different species and the high sensitivity on the presence of traces of protons (as discussed below).

Intuitively, we would have assumed that in the case of **Ir-NHI**, based on the redox potential and more particularly the low oxidation potential of the NHI moiety, rapid quenching of the ^{3}MLCT by intramolecular electron transfer could occur, which provides an alternative nonradiative deactivation pathway, but we could not find a spectroscopic proof for this. Hence, either this process is not occurring at all or only in a very minor overall contribution and/or the occurrence of this intermediate is too short to be detected with our spectroscopic methods. Due to the significantly shorter lifetime of the **Ir-NHI** a reactivity with a fast-intramolecular electron transfer from the NHI moiety and subsequent unproductive recombination escaping a spectroscopic detection cannot be excluded.

Spectroscopic analysis of the protonated **Ir-NHI.2H$^+$**, clearly indicates that upon protonation the influence of the NHI moiety can largely be suppressed. The absorption spectrum is providing weaker extinction coefficients in the UV range of the spectrum, which are significantly different from **Ir-NHI** and much closer to the unmodified **Ir-bpy** (Figure 5a-c). Similarly, the emission maximum is red-shifted compared to the **Ir-NHI** and significantly

prolonged, resulting in a maximum at 595 nm and a lifetime of 100 ns (Figure 5a-c and Table 1) close to the unmodified **Ir-bpy**.

Investigation by fs-TAS revealed that multiple processes are occurring and the seemingly monoexponential decay detectable by TCSPC method shows different intermediates to reach the final long-lived emissive $MLCT_{bpy}$ state (Figure 5f). Target analysis of the dataset indicates again two parallel deactivation pathways; a first one with a short-lived hot state of ~10 ps and around ~650 ps for the corresponding excited state, which is attributed to a $MLCT_{ppy}$ by comparison with the dataset from the **Ir-NHI** based on the broad absorption band up to 600 nm. Opposite to the **Ir-NHI**, in the protonated version the $MLCT_{bpy}$ state is again the lowest excited state and best fits were obtained with a model using the intermediate $MLCT_{ppy}$ with a lifetime of ~650 ps. Interestingly, while in the **Ir-bpy** the final $MLCT_{bpy}$-state is reached within the femtosecond time-scale, here this intermediate state has a longer lifetime. Analyzing the protonated complex by a kinetic map on the nanosecond timescale, a clean monoexponential decay is visible with absorption maximum in the UV around 380 nm and in the visible range around 500 nm with a lifetime of 100 ns (Figure 5i) (see SI section 6.6 Figure S55) which is in very good agreement with the long-lived component of the femtosecond dataset (Figure 5f) as well as the parent complex **Ir-bpy** (Figure 5d).

While the analysis is not straightforward between the different datasets and instruments with different detection methods and spectral ranges, a reasonable proposal for the different photophysical schemes is shown in Figure 6. For the case of **Ir-bpy**, the long-lived excited state is reached within the early picosecond timescale and the bpy-based MLCT has a long lifetime of several hundred nanoseconds under argon. In contrast, for **Ir-NHI** both bpy- and ppy-based MLCT states result in the long-lived $MLCT_{ppy}$, although presumably with much larger contributions from other deactivation pathways and thus a significantly smaller overall efficiency (Figure 6b). Pronating the NHI moiety again inverts the excited-state energies and the lowest excited state has again a $MLCT_{bpy}$ character.

In summary, by the combination of different spectroscopic techniques a change in the lowest excited state between **Ir-bpy** and **Ir-NHI** was identified, which could be inverted upon protonation of the NHI moiety. Plausible schemes for the excited-state deactivations based on the spectroscopic findings are presented in Figure 6.

3 | Conclusion

In this work, we introduced the novel N-heterocyclic imine (NHI)-functionalized bipyridine ligands as a new class of strongly electron-donating scaffold for the formation of Ir(III) complexes with switchable excited-state properties. This novel class of ligand could be straightforwardly obtained on a multi-gram scale. Electrochemical and spectroscopic studies revealed that NHI substitution destabilizes the LUMO and suppressed the classical bpy reduction. Steady-state and time-resolved spectroscopic titrations, carried out at very early time-scale, demonstrated the possibility to reversibly modulate the ground and excited-state properties of **Ir-NHI** through the addition of protons. The change in the excited-state nature with contributions from the ppy and bpy ligand indicates potentially new tuning possibilities with similar systems and changes on the ppy ligand scaffold. Our results demonstrate both the potential and challenges of leveraging strongly donating ligands in photoredox catalyst designs. Indeed, while NHI substitution allowed to tune the excited-state properties and pH switching abilities, it also introduced a sensitivity to dissolved oxygen upon exposure to light. Nevertheless, this novel ligand design opens the door for targeted photoredox applications, such as photodynamic therapy as cancerous cells operate in more acidic conditions as well as in the development of novel sensors.

Acknowledgments

This work was supported by the Fonds de la Recherche Scientifique (F.R.S.-FNRS) under CDR grant no. 40020332 (L.T.-G.). L.T.-G. is a Chercheur Qualifié of the Fonds de la Recherche Scientifique – FNRS. F.G. is a Chargé de Recherche of the Fonds de la Recherche Scientifique – FNRS. S.L., F.G. and L.T.-G. gratefully acknowledge the UCLouvain for financial support. S.L. acknowledges Abdullah Abudayyeh for assistance with initial electrochemical measurements. We acknowledge Kipras Redeckas, Greta Bučytė and Light Conversion for providing the opportunity to run a demo of HARPIA-LIGHT in our laboratory. We would like to thank Jonas Bohle and Valentin Wechselberger for contributing to the synthesis of the bpy-NHI ligand. J.H.F. thanks the Tiroler Wissenschaftsförderung (TWF, F.45075) for funding.

Conflicts of Interest

The authors declare no conflicts of interest.

References

1. M. H. Shaw, J. Twilton, and D. W. C. MacMillan, "Photoredox Catalysis in Organic Chemistry," *The Journal of Organic Chemistry* 81 (2016): 6898–6926.

2. J. Twilton, C. Le, P. Zhang, M. H. Shaw, R. W. Evans, and D. W. C. MacMillan, "The Merger of Transition Metal and Photocatalysis," *Nature Reviews Chemistry* 1 (2017): 0052.

3. K. A. Xie, E. Bednarova, C. L. Joe, et al., "Orange Light-Driven C(sp 2)–C(sp 3) Cross-Coupling via Spin-Forbidden Ir(III) Metallaphotoredox Catalysis," *Journal of the American Chemical Society* 145 (2023): 19925–19931.

4. D. N. Tritton, F.-K. Tang, G. B. Bodedla, et al., "Development and Advancement of Iridium(III)-Based Complexes for Photocatalytic Hydrogen Evolution," *Coordination Chemistry Reviews* 459 (2022): 214390.

5. K.-W. Lo, M.-W. Louie, and K. Y. Zhang, "Design of Luminescent Iridium(III) and Rhenium(I) Polypyridine Complexes as in Vitro and in Vivo ion, Molecular and Biological Probes," *Coordination Chemistry Reviews* 254 (2010): 2603–2622.

6. D. Jacquemin and D. Escudero, "The Short Device Lifetimes of Blue PhOLEDs: Insights Into the Photostability of Blue Ir(iii) Complexes," *Chem Sci* 8 (2017): 7844–7850.

7. J. C. Deaton, F. N. Castellano, and E. Zysman-Colman, *John Wiley & Sons Ltc* (2017): 1–69.

8. R. Bevernaegie, S. A. M. Wehlin, B. Elias, and L. Troian-Gautier, "A Roadmap Towards Visible Light Mediated Electron Transfer Chemistry With Iridium(III) Complexes," *ChemPhotoChem* 5 (2021): 217–234.

9. F. Monti, A. Baschieri, L. Sambri, and N. Armaroli, "Excited-State Engineering in Heteroleptic Ionic Iridium(III) Complexes," *Accounts of Chemical Research* 54 (2021): 1492–1505.

10. S. DiLuzio, V. Mdluli, T. U. Connell, J. Lewis, V. VanBenschoten, and S. Bernhard, "High-Throughput Screening and Automated Data-Driven Analysis of the Triplet Photophysical Properties of Structurally Diverse, Heteroleptic Iridium(III) Complexes," *Journal of the American Chemical Society* 143 (2021): 1179–1194.

11. C. Wang, L. Liu, W. Sun, et al., "Discovery of Novel Iridium(III) Complex-Based Photofunctional Materials Using Excited-State Descriptors," *Advanced Optical Materials* 13 (2025): 2402317.

12. Y. Suzuki, I. Imanishi, K. Shiba, et al., "pH- and Saccharide-Responsive Cyclometalated Iridium(III) Complexes With Boronic Acid Moieties Displaying a Wide Range of Phosphorescence Colors," *Chemistry—A European Journal* 31 (2025): e202404010.

13. E. S. Knorr, J. C. Kelly, D. P. Harrison, et al., "Bromo-Substituted Phenylbenzothiazole Cyclometalating Ligands for the Development of Reverse Saturable Absorption Materials," *Inorganic Chemistry* 64 (2025): 14952–14967.

14. C. Jacob, J. Annibaletto, and C. Theunissen, "Photoredox-Catalyzed Reductive Activation of Ammonium Salts," *Synlett* 36 (2025): 1729–1734.

15. J. D. Nguyen, E. M. D'Amato, J. M. R. Narayanam, and C. R. J. Stephenson, "Engaging unactivated alkyl, alkenyl and aryl iodides in visible-light-mediated free radical reactions," *Nature Chemistry* 4 (2012): 854–859.

16. J.-H. Shon and T. S. Teets, "Photocatalysis With Transition Metal Based Photosensitizers," *Comments on Inorganic Chemistry* 40 (2020): 53–85.

17. J.-H. Kim, S.-Y. Kim, Y.-J. Cho, H.-J. Son, D. W. Cho, and S. O. Kang, "A Detailed Evaluation for the Nonradiative Processes in Highly Phosphorescent Iridium(III) Complexes," *The Journal of Physical Chemistry C* 122 (2018): 4029–4036.

18. D. Ruggeri, M. Hoch, D. Spataro, et al., "Tuning the Efficiency of Iridium(III) Complexes for Energy Transfer (EnT) Catalysis Through Ligand Design," *Chemistry—A European Journal* 31 (2025): e202403309.

19. A. F. Henwood and E. Zysman-Colman, "Lessons Learned in Tuning the Optoelectronic Properties of Phosphorescent Iridium(iii) Complexes," *Chem Commun* 53 (2017): 807–826.

20. N. A. Till, L. Tian, Z. Dong, G. D. Scholes, and D. W. C. MacMillan, "Mechanistic Analysis of Metallaphotoredox C–N Coupling: Photocatalysis Initiates and Perpetuates Ni(I)/Ni(III) Coupling Activity," *Journal of the American Chemical Society* 142 (2020): 15830–15841.

21. V. Q. Dang and T. S. Teets, "Visible-Light Photohydrogenation of Ketones, Aldehydes, and Imines Using a Strongly Reducing Photosensitizer," *Organometallics* 43 (2024): 1698–1705.

22. Y. K. Radwan, A. Maity, and T. S. Teets, "Manipulating the Excited States of Cyclometalated Iridium Complexes With β-Ketoiminate and β-Diketiminate Ligands," *Inorganic Chemistry* 54 (2015): 7122–7131.

23. J.-H. Shon and T. S. Teets, "Potent Bis-Cyclometalated Iridium Photoreductants With β-Diketiminate Ancillary Ligands," *Inorganic Chemistry* 56 (2017): 15295–15303.

24. J.-H. Shon, S. Sittel, and T. S. Teets, "Synthesis and Characterization of Strong Cyclometalated Iridium Photoreductants for Application in Photocatalytic Aryl Bromide Hydrodebromination," *ACS Catalysis* 9 (2019): 8646–8658.

25. S. Ladouceur, D. Fortin, and E. Zysman-Colman, "Role of Substitution on the Photophysical Properties of 5,5′-Diaryl-2,2′-bipyridine (bpy*) in [Ir(ppy) 2 (bpy*)]PF 6 Complexes: A Combined Experimental and Theoretical Study," *Inorganic Chemistry* 49 (2010): 5625–5641.

26. M.-A. Tehfe, M. Lepeltier, F. Dumur, D. Gigmes, J.-P. Fouassier, and J. Lalevée, "Structural Effects in the Iridium Complex Series: Photoredox Catalysis and Photoinitiation of Polymerization Reactions Under Visible Lights," *Macromolecular Chemistry and Physics* 218 (2017): 1700192.

27. J. H. Franzen, L. F. B. Wilm, P. Rotering, K. Wurst, M. Seidl, and F. Dielmann, "Electron-rich pyridines With para -N-heterocyclic imine substituents: Ligand properties and coordination to CO 2 , SO 2 , BCl 3 and Pd II complexes," *Dalton Transactions* 53 (2024): 11876–11883.

28. J. H. Franzen, X. Zhou, K. Biv, et al., *Inorg Chem Front* (2025).

29. M. Zhong and M. Yuan, "Recent Advances in the use of N-Heterocyclic Carbene Adducts of N, P, C Elements as Supporting Ligands in Organometallic Chemistry," *RSC Advances* 15 (2025): 15052–15085.

30. D. Zhang, E. J. Dufek, and E. L. Clennan, "Syntheses, Characterizations, and Properties of Electronically Perturbed 1,1'-Dimethyl-2,2'-bipyridinium Tetrafluoroborates," *The Journal of Organic Chemistry* 71 (2006): 315–319.

31. L. Guo, H. Zhang, M. Tian, et al., "Electronic Effects on Reactivity and Anticancer Activity by Half-sandwich N,N-Chelated Iridium(iii) Complexes," *New Journal of Chemistry* 42 (2018): 16183–16192.

32. B. S. Uppal, A. Zahid, and P. I. P. Elliott, "Synthesis and Characterization of Azidobipyridyl Ruthenium Complexes and Their "Click" Chemistry Derivatives," *European Journal of Inorganic Chemistry* 2013 (2013): 2571–2579.

33. C. Hierlinger, A. K. Pal, F. Stella, et al., "Synthesis, Characterization, and Optoelectronic Properties of Iridium Complexes Bearing Nonconjugated Six-Membered Chelating Ligands," *Inorganic Chemistry* 57 (2018): 2023–2034.

34. P. Pyykkö and M. Atsumi, *Chem-Eur J* 15 (2009): 186–197.

35. P. Pyykkö and M. Atsumi, *Chem-Eur J* 15 (2009): 12770–12779.

36. Q. Teng and H. V. Huynh, "Determining the Electron-Donating Properties of Bidentate Ligands by 13 C NMR Spectroscopy," *Inorganic Chemistry* 53 (2014): 10964–10973.

37. Q. Teng and H. V. Huynh, "A Unified Ligand Electronic Parameter Based on 13 C NMR Spectroscopy of N-Heterocyclic Carbene Complexes," *Dalton Transactions* 46 (2017): 614–627.

38. T. U. Connell, C. L. Fraser, M. L. Czyz, et al., *J Am Chem Soc* 141 (2019): 17646–17658.

39. J. C. Bawden, P. S. Francis, S. DiLuzio, et al., *J Am Chem Soc* 144 (2022): 11189–11202.

40. L. Troian-Gautier, E. E. Beauvilliers, W. B. Swords, and G. J. Meyer, "Redox Active Ion-Paired Excited States Undergo Dynamic Electron Transfer," *Journal of the American Chemical Society* 138 (2016): 16815–16826.

41. S. A. M. Wehlin, L. Troian-Gautier, G. Li, and G. J. Meyer, "Chloride Oxidation by Ruthenium Excited-States in Solution," *Journal of the American Chemical Society* 139 (2017): 12903–12906.

42. S. A. M. Wehlin, L. Troian-Gautier, R. N. Sampaio, L. Marcélis, and G. J. Meyer, "Ter-Ionic Complex that Forms a Bond Upon Visible Light Absorption," *Journal of the American Chemical Society* 140 (2018): 7799–7802.

43. M. J. Goodwin, A. M. Deetz, P. J. Griffin, and G. J. Meyer, "Periodic Trends in Intra-ionic Excited State Quenching by Halide," *Inorganic Chemistry* 63 (2024): 15772–15783.

44. A. M. Deetz, M. J. Goodwin, E. A. Kober, and G. J. Meyer, "Nanosecond Intra-Ionic Chloride Photo-Oxidation," *Inorganic Chemistry* 62 (2023): 11414–11425.

45. P. D. Beer, F. Szemes, V. Balzani, et al., "Anion Selective Recognition and Sensing by Novel Macrocyclic Transition Metal Receptor Systems. 1 H NMR, Electrochemical, and Photophysical Investigations," *Journal of the American Chemical Society* 119 (1997): 11864–11875.

46. L. M. Hancock and P. D. Beer, "Chloride Recognition in Aqueous Media by a Rotaxane Prepared via a New Synthetic Pathway," *Chemistry—A European Journal* 15 (2009): 42–44.

47. N. H. Evans and P. D. Beer, "Advances in Anion Supramolecular Chemistry: From Recognition to Chemical Applications," *Angewandte Chemie International Edition* 53 (2014): 11716–11754.

48. I. Müller, C. Schneider, C. Pietzonka, F. Kraus, and C. G. Werncke, *Inorganics* 7 (2019): 117.

49. P. G. Shangin, I. V. Krylova, A. V. Lalov, et al., "Supramolecular D···A-layered structures based on germanium complexes With 2,3-dihydroxynaphthalene and N , N ′-bidentate ligands," *RSC Advances* 11 (2021): 21527–21536.

50. D. R. D. Pasi, P. T. Phanrang, D. Chamlagai, and S. Mitra, "Deciphering the Fluorescence Response of Structurally Diverse Nitrogen Containing Small Heterocycles: A Combined Experimental and Computational Approach," *Journal of Molecular Structure* 1335 (2025): 141841.

51. R. Bevernaegie, L. Marcélis, B. Laramée-Milette, et al., "Trifluoromethyl-Substituted Iridium(III) Complexes: From Photophysics to Photooxidation of a Biological Target," *Inorganic Chemistry* 57 (2018): 1356–1367.

52. K. Suzuki, A. Kobayashi, S. Kaneko, et al., "Reevaluation of Absolute Luminescence Quantum Yields of Standard Solutions Using a Spectrometer With an Integrating Sphere and a Back-Thinned CCD Detector," *Physical Chemistry Chemical Physics* 11 (2009): 9850.

53. R. Bevernaegie, L. Marcélis, A. Moreno-Betancourt, et al., "Ultrafast Charge Transfer Excited State Dynamics in Trifluoromethyl-Substituted Iridium(iii) Complexes," *Physical Chemistry Chemical Physics* 20 (2018): 27256–27260.

54. E. Pomarico, M. Silatani, F. Messina, et al., "Dual Luminescence, Interligand Decay, and Nonradiative Electronic Relaxation of Cyclometalated Iridium Complexes in Solution," *The Journal of Physical Chemistry C* 120 (2016): 16459–16469.

55. C. Lentz, L. Marcélis, L. Troian-Gautier, K. Robeyns, E. Cauët, and B. Elias, "Excited-State Behavior and Photoinduced Electron Transfer of pH-Sensitive Ir(III) Complexes With Cyclometallation (C/N–) Ratios Between 0/6 and 3/3," *Journal of Photochemistry and Photobiology A: Chemistry* 405 (2021): 112957.

56. P. Zhao, S. Tofighi, R. M. O'Donnell, et al., "Electronic Nature of New Ir(III) Complexes: Linear Spectroscopic and Nonlinear Optical Properties," *The Journal of Physical Chemistry C* 121 (2017): 23609–23617.

57. M. E. Olumba, R. M. O'Donnell, T. N. Rohrabaugh Jr., and T. S. Teets, "Panchromatic Excited-State Absorption in Bis-Cyclometalated Iridium Isocyanide Complexes," *Inorganic Chemistry* 61 (2022): 19344–19353.

58. K.-C. Tang, K. L. Liu, and I. C. Chen, "Rapid Intersystem Crossing in Highly Phosphorescent Iridium Complexes," *Chemical Physics Letters* 386 (2004): 437–441.

59. G. J. Hedley, A. Ruseckas, and I. D. W. Samuel, "Ultrafast Luminescence in Ir(ppy)3," *Chemical Physics Letters* 450 (2008): 292–296.

60. S. Ladouceur, D. Fortin, and E. Zysman-Colman, "Enhanced Luminescent Iridium(III) Complexes Bearing Aryltriazole Cyclometallated Ligands," *Inorganic Chemistry* 50 (2011): 11514–11526.

61. N. Kuhn and T. Kratz, "Synthesis of Imidazol-2-Ylidenes by Reduction of Imidazole-2(3 H)-thiones," *Synthesis* 1993 (1993): 561–562.

62. G. M. Sheldrick, "Crystal Structure Refinement With SHELXL," *Acta Crystallographica Section C Structural Chemistry* 71 (2015): 3–8.

63. G. M. Sheldrick, "SHELXT—Integrated Space-Group and Crystal-Structure Determination," *Acta Crystallographica Section A Foundations and Advances* 71 (2015): 3–8.

64. O. V. Dolomanov, L. J. Bourhis, R. J. Gildea, J. A. K. Howard, and H. Puschmann, "OLEX2: A Complete Structure Solution, Refinement and Analysis Program," *Journal of Applied Crystallography* 42 (2009): 339–341.

65. C. I. G. Diamond, 1997–2022, Version 4.6.8.

Supporting Information

Additional supporting information can be found online in the Supporting Information section.

The authors have cited additional references within the Supporting Information [60–65]. The supporting Information contains additional experiments, NMR characterization and well as photophysical characterization. Crystallographic data have been deposited with the Cambridge Crystallographic Data Centre as supplementary publication no. CCDC- 2494761 (**bpy-NHI**) and CCDC- 2494762 (**bpy-NHI•3HOTf**).

Supporting file 1: chem70576-sup-0001-SuppMat.pdf
Supporting file 2: chem70576-sup-0002-DataFile.zip